ACS Energy LETTERS

http://pubs.acs.org/journal/aelccp

Chemical Modulation of Local Transition Metal Environment Enables Reversible Oxygen Redox in Mn-Based Layered Cathodes

Muhammad Mominur Rahman, Scott McGuigan, Shaofeng Li, Lina Gao, Dong Hou, Zhijie Yang, Zhengrui Xu, Sang-Jun Lee, Cheng-Jun Sun, Jue Liu, Xiaojing Huang, Xianghui Xiao, Yong Chu, Sami Sainio, Dennis Nordlund, Xueqian Kong, Yijin Liu, and Feng Lin*

Cite This: *ACS Energy Lett.* 2021, 6, 2882–2890

Read Online

ACCESS | Metrics & More | Article Recommendations | Supporting Information

ABSTRACT: **Oxygen redox plays a prominent role in enhancing the energy density of Mn-based layered cathodes. However, understanding the factors affecting the reversibility of oxygen redox is nontrivial due to complicated structural and chemical transformations. Herein, we show that local Mn−O symmetry induced structural/chemical evolutions majorly dictate the reversibility of oxygen redox of $Na_xLi_yMn_{1-y}O_2$ in Na cells. $Na_xLi_yMn_{1-y}O_2$ with Jahn−Teller distorted MnO_6 octahedra undergoes severe Mn dissolution during cycling, which destabilizes the transition metal layer resulting in poor Li retention and irreversible oxygen redox. Jahn−Teller distortion of MnO_6 octahedra can be suppressed by modulating the local charge of Mn and Mn−O distance through Mg/Ti dual doping. This leads to reduced Mn dissolution and more reversible oxygen redox. Such stabilization significantly improves the electrochemical performance of Mg/Ti dual doped $Na_xLi_yMn_{1-y}O_2$. Through this work, we show that local structural stabilization through local chemical environment modification can promote reversible oxygen redox in layered cathodes.**

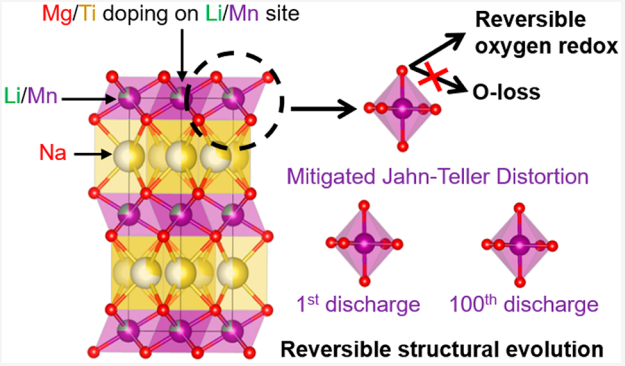

Oxygen redox can break the limited energy density barrier of layered cathodes, which gives opportunities to develop high energy cathode materials for alkali-ion batteries.[1,2] Oxygen redox is widely studied in Li-rich layered oxides ($Li[Li_xTM_{1-x}]O_2$, where TM stands for transition metal ions).[3,4] In Li-rich layered oxides, unhybridized O 2p orbitals form along the Li−O−Li configurations with Li sitting in both transition metal layer and interlayer.[5] These O 2p orbitals are higher in energy than the bonding molecular orbitals but lower in energy than the antibonding molecular orbitals, putting them closer to the Fermi level than the hybridized O 2p states. Hence, the unhybridized O 2p orbitals are redox active in these materials. Similarly, Na−O−Li and Na−O−Mg configurations are created in sodium layered oxides with 3d transition metals upon substitution of some transition metals by Li or Mg.[6,7] O 2p orbitals in these configurations are also unhybridized and thus, redox active.[8]

Development of layered oxide cathodes with oxygen redox has faced many hurdles. One such hurdle is the irreversible oxygen redox, which often leads to many unwanted phenomena such as electrolyte decomposition and gas evolution.[3] The gas evolution can cause the collapse of the crystal structure leading to the formation of cation dense phase.[9,10] Alkali/alkaline ions in the transition metal layer that are responsible for triggering oxygen redox,[11] play a dominant role in determining the oxygen redox reversibility. Bruce and co-workers have shown that Li loss from the transition metal layer of $Na_xLi_yMn_{1-y}O_2$ at high states of charge leads to the formation of underbonded oxygen ions causing O_2 and CO_2 evolution.[11] Many studies have shown that local Li environment in the transition metal layer of Li-substituted Na layered oxides can be in dynamic evolution between the transition metal layer and the interlayer at different stages of cycling.[11−13] The interlayer space provides open channels for Li transport

Received: May 26, 2021
Accepted: July 20, 2021
Published: July 26, 2021

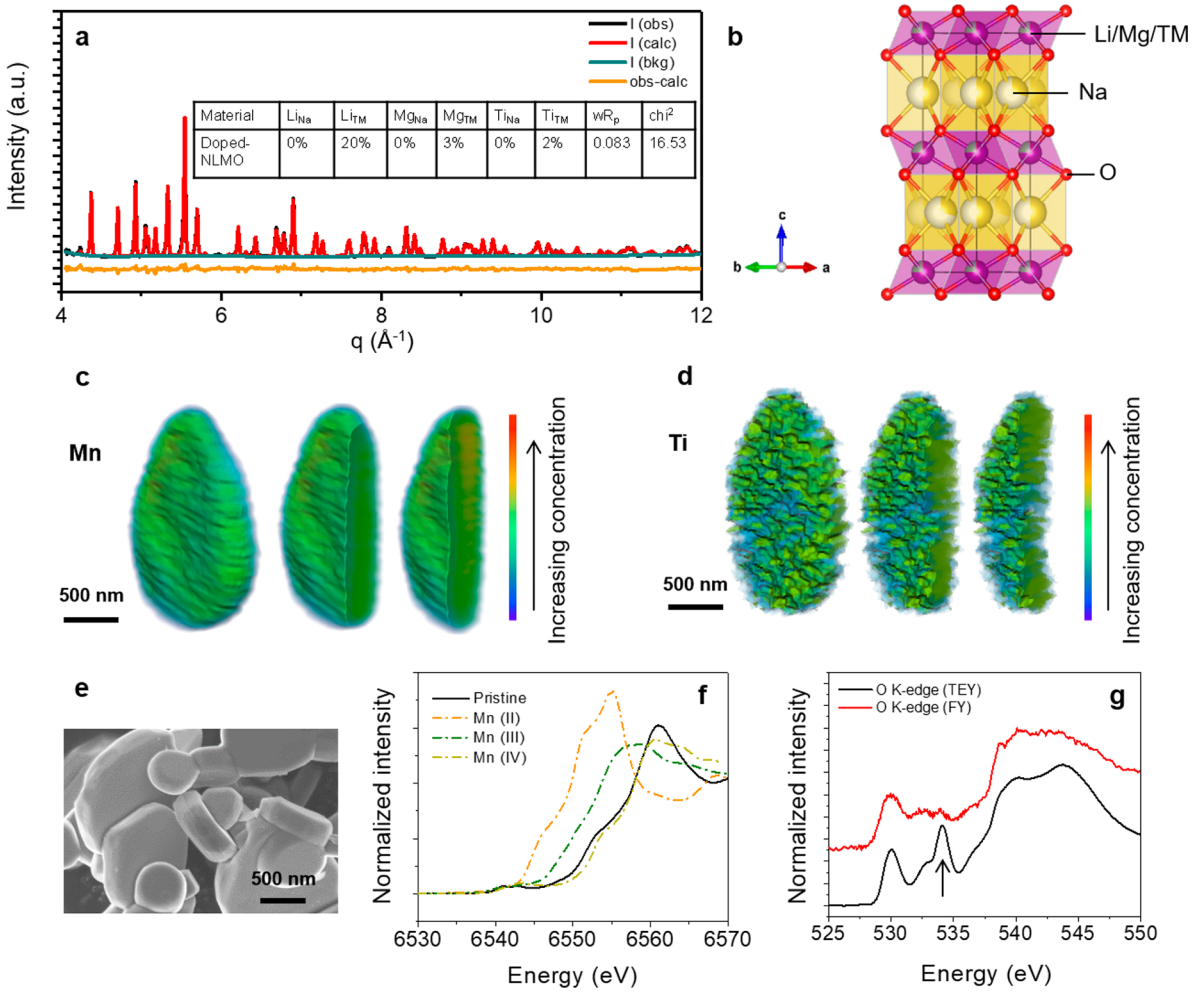

Figure 1. Physicochemical characterization of the pristine $Na_{0.8}Li_{0.2}Mg_{0.03}Ti_{0.02}Mn_{0.75}O_2$ (doped-NLMO). (a) Neutron diffraction pattern with Rietveld refinement. The pattern is refined with a $P6_3/mmc$ space group to figure out the preferred lattice sites the dopants (Mg and Ti) and other elements (Li and Mn) occupy. The table in the inset shows the occupancy of the elements in either the transition metal layer (TM) or the interlayer (Na) of the crystal structure shown in (b). (b) Crystal structure of $Na_{0.8}Li_{0.2}Mg_{0.03}Ti_{0.02}Mn_{0.75}O_2$ showing the lattice sites various elements (Li, Mg, Ti, Mn, Na, and O) prefer to occupy. TM in the structure stands for transition metals (Mn or Ti). (c) 3D fluorescence tomograph of Mn. The color bar shows the relative distribution of Mn in each voxel. (d) 3D fluorescence tomograph of Ti. The color bar shows the relative distribution of Ti in each voxel. (e) SEM image of the pristine particles of $Na_{0.8}Li_{0.2}Mg_{0.03}Ti_{0.02}Mn_{0.75}O_2$. (f) Mn K-edge XANES spectrum of $Na_{0.8}Li_{0.2}Mg_{0.03}Ti_{0.02}Mn_{0.75}O_2$ in the pristine state. The spectra with dotted lines are for Mn in +2 (MnO), +3 (Mn_2O_3), and +4 (MnO_2) oxidation states. (g) O K-edge XAS spectra in total electron yield (TEY) mode and fluorescence yield (FY) mode for pristine $Na_{0.8}Li_{0.2}Mg_{0.03}Ti_{0.02}Mn_{0.75}O_2$. The peak marked by the arrow originates due to the presence of carbonate and/or bicarbonate species.

out of the material, leading to Li loss. Hence, enhancing the reversibility of local Li environment is a key factor for stabilizing oxygen redox. In addition, local transition metal environment provides challenges that can compound the instability issues related to the local Li environment. Local structural distortion surrounding transition metal ions causes lattice stress development, which is detrimental to the electrochemical performance.[14] Mn plays a critical role in both redox reaction[15] and structural transformation in oxygen redox active Mn-based layered cathodes. Mn containing layered oxides often show Jahn−Teller distortion[14] and such distortion aggravates Mn dissolution from the cathode.[16] The accelerated Mn dissolution may cause Li loss and degradation of the transition metal layer that can negatively impact the reversibility of oxygen redox. Doping chemistry has been widely utilized to suppress Jahn−Teller distortion. For example, Mg doping enhances the phase stability through breaking the alkali ion/vacancy ordering and suppress Jahn−Teller distortion through raising the local charge of Mn ions.[17−19] Ti doping can suppress Jahn−Teller distortion through reducing the bond length variation along the axial and equatorial directions.[14,20] Ti dopant is also known to enhance oxygen retention in layered oxides due to its strong chemical bonding with oxygen.[21,22] Such structural stabilization through doping chemistry may also be beneficial toward the reversibility of the oxygen redox process. Hence, a well-informed connection between the role of local structural reversibility of Mn and Li and that of oxygen redox may lead to the stabilization of oxygen redox in Mn-based layered cathodes.

In this study, we show a direct correlation between the local Mn and Li environment and oxygen redox. We utilize Mg/Ti dual dopants on $Na_xLi_yMn_{1-y}O_2$ as a tool to impart the local Mn structural stability. Our study on $Na_xLi_yMn_{1-y}O_2$ and Mg/

https://doi.org/10.1021/acsenergylett.1c01071
ACS Energy Lett. 2021, 6, 2882−2890

Ti dual doped $Na_xLi_yMn_{1-y}O_2$ shows that Mg/Ti dual doping can suppress Jahn−Teller distortion and make the local Mn environment more reversible during electrochemical cycling. Such local structural reversibility of Mn leads to suppressed Mn dissolution, stabilizing the Mn layer. This results in stabilization of local Li environment and better overall Li retention. The combined reversibility of the local Mn and Li environment enhances the stability of oxygen redox in Mg/Ti dual doped $Na_xLi_yMn_{1-y}O_2$, which significantly improves the electrochemical performance in Na cells.

$Na_xLi_yMn_{1-y}O_2$ is synthesized through a solid-state synthesis method. The phase purity of the material depends closely on the ratio of Na and Li, indicating that Na and Li have a limited solubility (Figure S1). An excess of Li above the solubility leads to the formation of Li_2MnO_3 phase. An excess of Na above the solubility leads to the formation of Na_3MnO_4 phase, in line with reports by Komaba and co-workers (Figure S1).[23] By tuning the composition to $Na_{5/6}Li_{1/4}Mn_{3/4}O_2$ (mentioned as NLMO hereafter), a phase pure P2-type layered oxide can be obtained (Figure S2). Mg/Ti dual doped $Na_xLi_yMn_{1-y}O_2$ is synthesized through a coprecipitation method followed by high temperature calcination (details in the materials and methods section). By tuning the composition ($Na_{0.8}Li_{0.2}Mg_{0.03}Ti_{0.02}Mn_{0.75}O_2$; mentioned as doped-NLMO hereafter) and calcination condition (850 °C for 10 h followed by natural furnace cooling), a phase pure material with P2-type crystal structure can be obtained (Figure S3). Crystal structure of both materials can be defined by a hexagonal lattice with $P6_3/mmc$ space group, isostructural to P2−Na_xCoO_2 (Figure S4).[24] An additional reflection is observed in the patterns which indicates Li/Mn honeycomb ordering in the transition metal layer (corresponding to (1/3 1/3 1) crystal plane in Figure S4).[11,23] Rietveld refinement on neutron diffraction patterns is performed to figure out the specific lattice sites the constituent elements prefer to occupy (Figure 1a and Figure S2). Our refinement shows that both Mg and Ti share occupancy with Mn in the transition metal layer (Figure 1b and Table S1). While all Li sits in the transition metal layer in doped-NLMO (Figure 1b and Table S1), 5% Li sits in the Na layer in NLMO (Table S1). Lattice parameters derived from the Rietveld refinement are reported in Table S2. Doped-NLMO has larger c parameter (11.0660 Å) than NLMO (11.0135 Å). The higher Na content of NLMO may lead to greater suppression of the repulsion between the transition metal layer in comparison to doped-NLMO, which can decrease the c parameter of the unit cell. Dopant distribution in doped-NLMO is performed through scanning electron microscopy-energy dispersive X-ray spectroscopy (SEM-EDS images in Figure S5) and 3D fluorescence tomography (Figure 1c and 1d). SEM-EDS is performed on bulk exposed doped-NLMO particles. The bulk of the particles are exposed through a polishing method (details in the materials and methods section). The SEM-EDS images on multiple particles of doped-NLMO show that both Mg and Ti are present throughout the particles (Figure S5). This is further supported by the 3D fluorescence tomographs of Mn and Ti (Figure 1c and 1d) which show that Ti is present within the entire individual particle. The 3D distribution of Ti on the individual particle is somewhat heterogeneous (Figure 1d), which is similar to Ti distribution in Li layered oxides.[17,25] However, Ti shares the same lattice site with Mn, Mg, and Li to form a single phase P2-type crystal structure (Figure 1a and 1b). We have not reported the fluorescence tomograph of Mg because of significant self-absorption of Mg fluorescence signal. Particles of NLMO and doped-NLMO have random to hexagonal plate type morphology (Figure S6 and Figure 1e). The bulk oxidation state of Mn in doped-NLMO is evaluated through hard X-ray absorption spectroscopy (Figure 1f). Pre-edge region of Mn K-edge is compared to evaluate the oxidation state.[26] The bulk oxidation state of Mn is little lower than +4 (Figure 1f and Figure S7a), which is consistent with the oxidation state determined from the molecular formula of doped-NLMO (+3.81). Meanwhile, the oxidation state of Mn in NLMO is little lower than +4 (Figure S7b), which is also consistent with the calculated oxidation state from the molecular formula of NLMO (+3.89). The chemical environment of oxygen is probed through O K-edge spectra in total electron yield (TEY) mode and fluorescence yield (FY) mode. At the pristine state, O K-edge shows a pre-edge feature (at around 530 eV−533 eV) originating from the transition of electrons from O 1s orbital to the vacant states of the TM 3d−O 2p hybridized orbitals (Figure 1g). Surface region shows carbonate species, which decreases at the subsurface region of the doped-NLMO particle (compare the intensity of the peak marked by an arrow in Figure 1g).

To determine the role of oxygen redox in the charge/discharge process, it is important to understand the detailed charge compensation mechanism during electrochemical cycling. Mn K-edge XANES spectra are collected during the first cycle of doped-NLMO and NLMO at C/10 rate (Figure 2a and Figure S8). The small blue shift of the Mn K-edge during the charging process indicates that there is little oxidation of Mn during the first charge of both NLMO (Figure S8) and doped-NLMO (Figure 2a). To monitor the oxygen redox process, oxygen K-edge resonant inelastic X-ray scattering (RIXS) maps are collected at the charged states of doped-NLMO and NLMO (Figure 2b−2d and Figure S9). O K-edge RIXS has become the tool of choice to ascertain oxygen redox.[27] RIXS maps can differentiate the signal due to the lattice oxygen redox through resolving the energy of the emitted photons against the excitation energy.[28,29] Such resolution has revealed a unique signal at around 523.7 eV emission energy against a 531 eV excitation energy (marked by the red arrow within the white boxed region of Figure 2c). This signal has been revealed to originate from the oxidation of lattice oxygen during the charging process.[30] O K-edge RIXS maps of the charged (4.5 V) doped-NLMO shows a clear signal due to the lattice oxygen redox (marked by the red arrow in Figure 2c), which is not present in the pristine state (Figure 2b). This proves the participation of lattice oxygen toward redox reaction during cycling. We also utilize O K-edge RIXS to probe the reversibility of oxygen redox in NLMO and doped-NLMO. After 51st charge, the signal of oxygen redox is still present in the O K-edge RIXS map of doped-NLMO (Figure 2d). Excitation spectra derived from integrating the signal along the excitation energy regime on the boxed region in Figure 2b and 2c show an increased intensity at 531 eV excitation energy (marked by the black arrow in Figure 2e) on first charge to 4.5 V. That increased intensity is still maintained after 51st charge (Figure 2e), indicating a reversible oxygen redox process. However, one can notice a slightly weaker signal due to oxygen redox in NLMO after comparing the O K-edge RIXS maps of 51st charge doped-NLMO and NLMO (Figure S9a,b). The intensity of the spectral feature at 531 eV is also decreased at 51st charge of NLMO in comparison to doped-NLMO (Figure S9c). Overall, our detailed charge compensa-

https://doi.org/10.1021/acsenergylett.1c01071
ACS Energy Lett. 2021, 6, 2882−2890

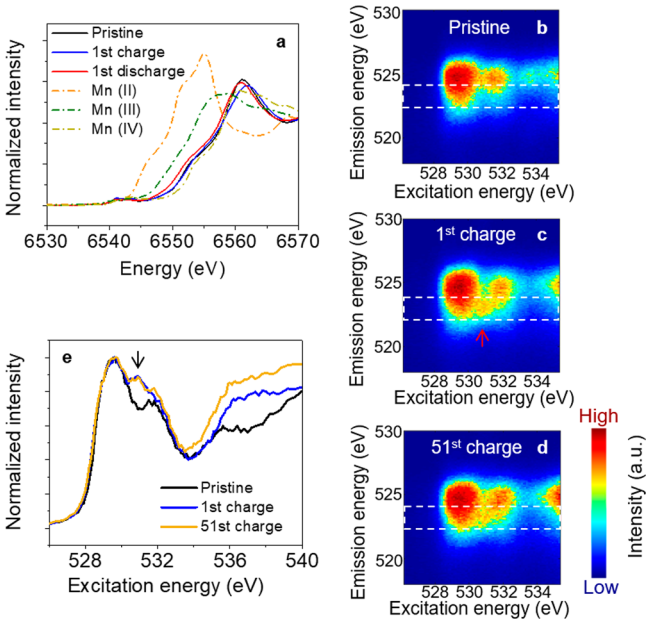

Figure 2. Charge compensation mechanism of $Na_{0.8}Li_{0.2}Mg_{0.03}Ti_{0.02}Mn_{0.75}O_2$ (doped-NLMO) during electrochemical cycling. (a) Mn K-edge XANES spectra in the first cycle (pristine, first charge to 4.5 V, and first discharge to 1.5 V). Cycling is performed at the C/10 rate. The dotted spectra are for standard Mn K-edges at +2 (MnO), +3 (Mn_2O_3), and +4 oxidation states (MnO_2). Oxygen K-edge resonant inelastic X-ray scattering (RIXS) map at (b) pristine state, (c) 1st charge, and (d) 51st charge. The color bar shows the intensity of the emitted photons in arbitrary units. The 1st charge is performed at the C/10 rate. Subsequent cycling is performed at the 1C rate followed by the 51st charge at the C/10 rate. The red arrow in Figure 2c indicates the signal originating due to oxygen redox. (e) Excitation spectra of the RIXS maps in (b−d). The excitation spectra are derived from the integration of the signal in the vertical direction on the boxed region of RIXS maps in (b−d).

tion study shows that lattice oxygen takes part in redox reactions in both materials and the oxygen redox is more reversible in doped-NLMO than the undoped counterpart.

We study the local Li and Mn structural evolution in detail to rationalize the observed oxygen redox reversibility in doped-NLMO. Magnitude of the Fourier transformed Mn K-edge extended X-ray absorption fine structure (EXAFS) spectra shows two main peaks (Figure 3a). The peak at around 1.5 Å originates due to the single scattering of photoelectrons by nearest neighboring oxygen scatterer. The peak at around 2.5 Å originates due to the single scattering of photoelectrons by either Mn or Li scatterer in NLMO or Mn, Ti, Mg, or Li scatterer in doped-NLMO. However, the scattering intensity from Li is negligible due to the lighter mass of Li. We perform fitting on the magnitude of the Fourier transformed Mn K-edge EXAFS spectra of NLMO (Figure S10). Fitting is performed in ARTEMIS software package, which utilizes FEFF to theoretically calculate the scattering pathways.[31] Three single scattering pathways, namely, equatorial Mn−O, axial Mn−O, and Mn−Mn, are chosen for the fitting as they contribute most to the first two shells of the Fourier transformed EXAFS spectrum (Figure S11). The fitting shows an elongation in Mn−O bond length along the axial direction and contraction along the equatorial direction in the pristine state and after long-term cycling (Figure S10 and Table S3). Jahn−Teller distorted MnO_6 octahedra are reported to be detrimental to the electrochemical performance, leading to Mn dissolution because of the more basic nature of the elongated axial Mn−O bond.[16] Indeed, NLMO has much larger Mn dissolution in comparison to doped-NLMO on electrochemical cycling (Figure S12 and Table S4). The instability of the transition metal layer originating from Jahn−Teller distortion and Mn dissolution also leads to Li loss from NLMO upon long-term cycling (66.6% retention after 50 cycles at C/5 rate in Figure S13). Simultaneous loss of both Li and Mn from the transition metal layer can lead to the deterioration of the transition metal layer and formation of severely underbonded oxygen ions, which can impact the reversibility of oxygen redox. Dahn and co-workers reported the formation of underbonded oxygen ions due to the loss of Li from $Na_xLi_yMn_{1-y}O_2$, leading to irreversible oxygen redox.[11] However, doping with Mg and Ti in doped-NLMO effectively suppresses Jahn−Teller distortion and makes the local MnO_6 evolution more reversible on electrochemical cycling (Figure 3a). Mn−O distance determined through the fitted Fourier transformed Mn K-edge EXAFS spectra shows that Jahn−Teller distortion in MnO_6 octahedra is suppressed in the pristine state (Figure 3a and 3b and Table S5). The evolution of the MnO_6 octahedra is also reversible on long-term electrochemical cycling. The suppression of Jahn−Teller distortion can originate from the cooperative effect of Mg and Ti doping. Mg doping can locally enhance the charge of Mn, reducing Jahn−Teller distortion.[19] Ti doping can reduce the Mn−O bond length variations along the axial and equatorial directions, leading to the suppression of Jahn−Teller distortion.[20] Ti can also strengthen the transition metal (TM)−O bond through decreasing the covalency which can enhance oxygen retention.[21,22] This leads to a reversible local Mn structural evolution in doped-NLMO. Suppressing Jahn−Teller distortion leads to less Mn dissolution on long-term cycling of doped-NLMO (Figure S12 and Table S4). Such reduced Mn dissolution will inevitably stabilize the transition metal layer and global Li retention on long-term cycling is also improved in comparison to NLMO as a result (81.8% Li retention after 50 cycles at the C/5 rate in Figure 3c). We probe the local Li environment in doped-NLMO closely with ^{7}Li projection magic angle turning-phase adjusted sideband separation (pj-MATPASS) NMR. The spectra show a major peak at a chemical shift bit larger than 2000 ppm with a small shoulder on the lower chemical shift (Figure 3d). The major peak originates for the Li surrounded by 6 Mn ions. The shoulder forms when in addition to Mn, Li is also surrounded by Ti or Mg in the second coordination shell.[32] No accumulation of Li in the interlayer is observed from the ^{7}Li NMR spectra in the pristine state and after long-term cycling as there is no peak lower than 1000 ppm chemical shift in Figure 3d.[11] Therefore, for both pristine and 50 cycles, the main peak and the shoulder in the NMR spectra (Figure 3d) can be accounted for Li sitting on the transition metal layer. Even after long-term cycling, all Li can still be found in the transition metal layer with no accumulation of Li in the interlayer. Meanwhile, many studies show the accumulation of Li in the interlayer space of Li substituted Na layered oxides on electrochemical cycling.[12,13] The interlayer space provides an open channel for Li migration out of the material, which can cause permanent Li loss on electrochemical cycling. Overall, the stable local Li and Mn environment in doped-NLMO ensures that there is less accumulation of Li in the interlayer.

https://doi.org/10.1021/acsenergylett.1c01071
ACS Energy Lett. 2021, 6, 2882−2890

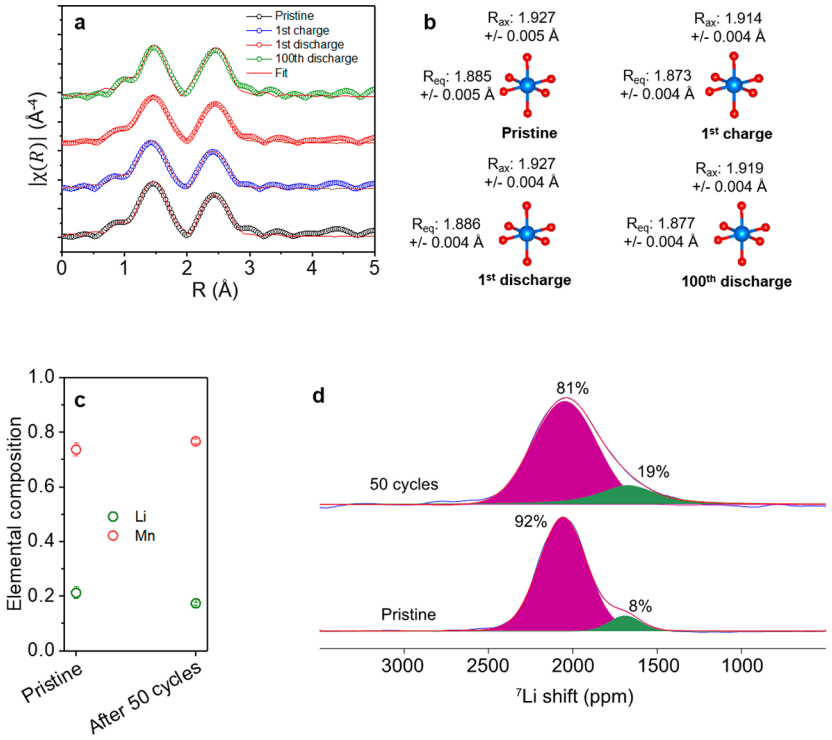

Figure 3. Local Mn and Li structural evolution in $Na_{0.8}Li_{0.2}Mg_{0.03}Ti_{0.02}Mn_{0.75}O_2$ (doped-NLMO) during initial and long-term cycling. (a) Magnitude of the fitted Fourier transformed Mn K-edge EXAFS spectra at different stages of cycling. The cycling is performed at the C/10 rate. (b) The evolution of Mn−O distances during different stages of cycling determined from the EXAFS fitting in (a). R_{eq} represents four Mn−O distances in the equatorial direction of the MnO_6 octahedron. R_{ax} represents two Mn−O distances in the axial direction of the MnO_6 octahedron. Red spheres are for oxygen while the blue spheres are for Mn. (c) Quantification of Li in the material through ICP-MS in the pristine state and after 50 cycles. The cycling is performed at the C/5 rate. The error bars are included with the data points. (d) ^{7}Li pj-MATPASS NMR spectra in the pristine state and after 50 cycles. The cycling is performed at the C/5 rate.

This along with reduced Mn dissolution can stabilize the transition metal layer, which helps sustain oxygen redox on long-term cycling. Reversible oxygen redox also leads to stable interfacial chemistry as observed through O K-edge spectra in FY mode. After 100 cycles at C/10, a carbonate-like species is observed in NLMO whereas no such species can be seen in doped-NLMO (peak marked by the arrow in Figure S14). This indicates a greater decomposition of the electrolyte to form carbonate species on NLMO which can be facilitated by the less reversible oxygen redox in NLMO.[33]

Reversible local structural evolution and oxygen redox lead to significant improvement in electrochemical performance of doped-NLMO in comparison to NLMO (Figure 4 and Figure S15). Doped-NLMO delivers an initial discharge capacity of 210 mAh/g at the C/10 rate (Figure 4a) and 145 mAh/g at the 1C rate (Figure 4b). In comparison, NLMO delivers an initial discharge capacity of 221 mAh/g at the C/10 rate (Figure S15a) and 151 mAh/g at the 1C rate (Figure S15b). NLMO delivers comparable capacity to similar $Na_xLi_yMn_{1-y}O_2$ materials (similar or different x/y ratios) reported in the literature.[23,34,35] Upon doping with 3% Mg, the cycling curves become smoother than NLMO and 2% Ti doped NLMO (Figure S16). This indicates Mg doping may enable breaking the alkali-ion/vacancy ordering on cycling.[17] Doping with either Mg or Ti improves the capacity retention at 1C (Figure S17). However, optimum capacity retention is observed when NLMO is doped with both Mg and Ti, indicating a cooperative stabilization of the material through Mg/Ti dual doping. In comparison to NLMO, the capacity retention is substantially improved in doped-NLMO at both C/10 and 1C rates (Figure 4c and Figure S15c). Likewise, energy retention is also stabilized in doped-NLMO (Figure S15d and Figure S18a). A stable Coulombic efficiency is delivered by doped-NLMO (Figure 4c) in comparison to NLMO (Figure S15e). A comparable average voltage is delivered by both materials at C/10 and 1C but more stable average voltage is delivered by doped-NLMO (Figure S15f and Figure S18b). Doping of Mg and Ti in NLMO can also slow down the lowering of the output voltage at faster C-rates (Figure 4d, Figure S15g). Doped-NLMO delivers an average voltage of 2.57 V at 1C (180 mA/g current density) whereas NLMO delivers 2.25 V average voltage at 1C. Even at 5C (900 mA/g), the average voltage of doped-NLMO (2.31 V) is higher than NLMO at 1C (2.25 V). The CV profile of both materials at 0.1 mV/s scan rate shows a peak at 4.38 V on the direction of positive voltage sweep in the first and second cycle, which can be attributed to high-voltage phase transformation (Figure S15h and Figure S18c).[36] This peak is observed even after cycling for 100 cycles at 1C (Figure 4e) when scanned at the same scanning rate, even though a decrease in peak height can be seen. However, the peak quickly diminishes in NLMO after cycling for just 50 cycles at 1C and replaced by a solvent oxidation peak (Figure S19), indicating an irreversible phase transformation process. The overall improvement of the electrochemical performance and the reversibility of oxygen redox reaction also led to stable interfacial processes in doped-NLMO. Figure S14 shows that NLMO undergoes more severe interfacial side reactions with carbonate-based surface products. This leads to significant development of interfacial charge transfer resistance in NLMO in comparison to doped-NLMO (Figure S15i and Figure

https://doi.org/10.1021/acsenergylett.1c01071
ACS Energy Lett. 2021, 6, 2882−2890

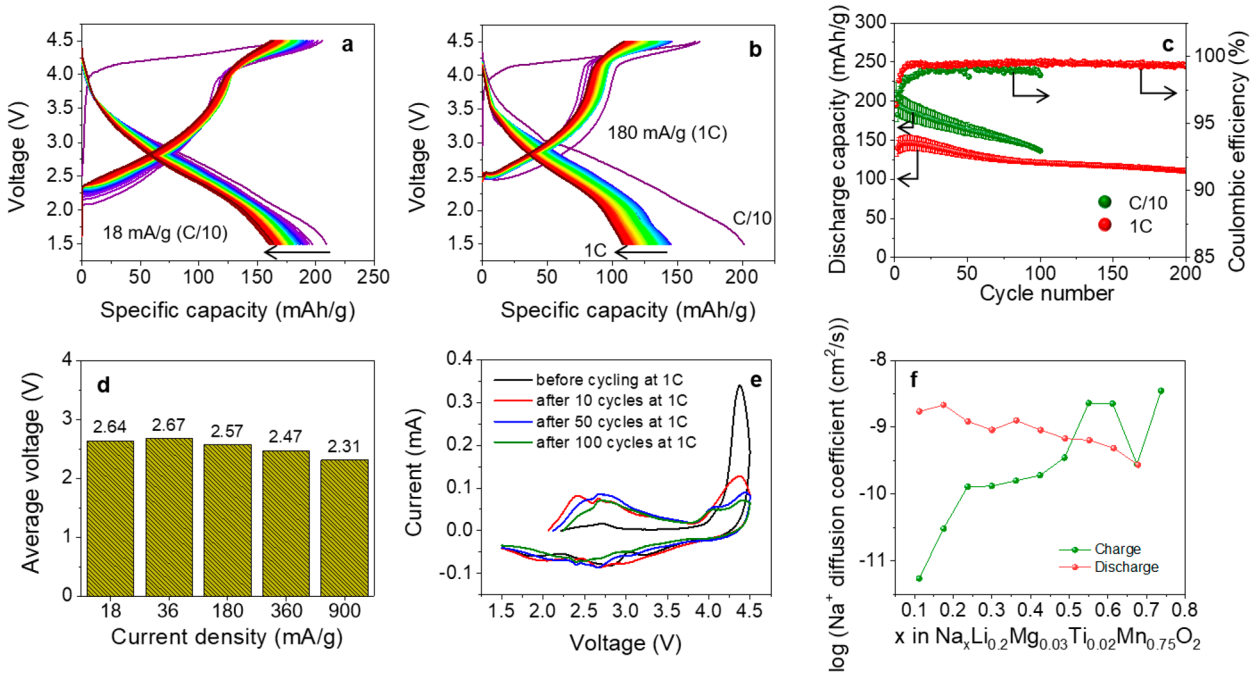

Figure 4. Electrochemical characterization of $Na_{0.8}Li_{0.2}Mg_{0.03}Ti_{0.02}Mn_{0.75}O_2$ (doped-NLMO). (a) Charge and discharge curves plotted for up to 100 cycles of the Na cell containing $Na_{0.8}Li_{0.2}Mg_{0.03}Ti_{0.02}Mn_{0.75}O_2$ as the cathode material at the C/10 rate within the voltage window of 1.5−4.5 V. The arrow indicates the direction the charge/discharge curves evolve from the 1st to 100th cycle. (b) Charge and discharge curves plotted for up to 200 cycles of Na cell containing $Na_{0.8}Li_{0.2}Mg_{0.03}Ti_{0.02}Mn_{0.75}O_2$ as the cathode material at the 1C rate within the voltage window of 1.5−4.5 V. The first cycle is performed at the C/10 rate. The arrow indicates the direction the charge/discharge curves evolve from the 1st to 200th cycle. (c) Capacity retention and Coulombic efficiency against cycle numbers at C/10 and 1C rates of $Na_{0.8}Li_{0.2}Mg_{0.03}Ti_{0.02}Mn_{0.75}O_2$ in Na cell. The capacity retentions and Coulombic efficiency are averaged from multiple cells. (d) Average voltage at different current densities delivered by $Na_{0.8}Li_{0.2}Mg_{0.03}Ti_{0.02}Mn_{0.75}O_2$. (e) Cyclic voltammogram of $Na_{0.8}Li_{0.2}Mg_{0.03}Ti_{0.02}Mn_{0.75}O_2$ before and after cycling for various cycles at 1C. The scanning is performed at 0.1 mV/s within 1.5−4.5 V. (f) Apparent Na^+ diffusion coefficient calculated from the GITT measurement. GITT measurement is performed at the C/10 rate with 1 h of constant current pulse followed by 10 h of open circuit relaxation.

S18d).[37] Kinetic measurement is performed through galvanostatic intermittent titration technique (Figure 4f).[38] The apparent Na^+ diffusion coefficient of doped-NLMO during charging ranges from 5.43×10^{-12} to 2.25×10^{-9} cm^2/s (Figure 4f). The diffusion coefficient during the discharge process varies from 9.08×10^{-10} to 1.22×10^{-9} cm^2/s (Figure 4f). Meanwhile, the apparent Na^+ diffusion coefficient of NLMO during the charging process ranges from 2.94×10^{-11} to 3.53×10^{-8} and 1.56×10^{-11} to 1.08×10^{-9} during discharging (Figure S20). Overall, the detailed electrochemical performance evaluation shows that making the local structural evolution of transition metals more reversible not only leads to stable oxygen redox but also substantially improves the electrochemical performance.

In summary, our work shows the critical role that the local structural environment in the transition metal layer plays to stabilize oxygen redox in Mn-based layered oxide cathodes. Li substitution in the transition metal layer can trigger oxygen redox due to the formation of unhybridized O 2p orbitals. However, the instability of Li and transition metal in the transition metal layer can make the oxygen redox process less reversible. We probe the local structural environment of Mn in $Na_{5/6}Li_{1/4}Mn_{3/4}O_2$ and observe Jahn−Teller distortion in MnO_6 octahedra through EXAFS analysis. The distortion causes severe Mn dissolution upon long-term cycling. The instability of Mn leads to Li loss, irreversible oxygen redox process, and unstable electrochemical performance. Mn dissolution can be suppressed by reducing the Jahn−Teller distortion through chemical modulation of local Mn environment by Mg and Ti dual doping. Such stabilization of the transition metal layer causes better Li retention and stable local Li environment with no Li accumulation in the interlayer as probed through ^7Li pj-MATPASS NMR (no peak at lower than 1000 ppm chemical shift in Figure 3d). As a result, a reversible oxygen redox process is observed through RIXS. Overall, the more reversible local Li and Mn environment and stable oxygen redox significantly improves the electrochemical performance of $Na_{0.8}Li_{0.2}Mg_{0.03}Ti_{0.02}Mn_{0.75}O_2$. This work provides a fundamental mechanistic understanding on the interplay between local Li and Mn environments and oxygen redox as well as showcases that stabilizing local environment in the transition metal layer is a promising pathway for stable oxygen redox.

■ ASSOCIATED CONTENT

Supporting Information

The Supporting Information is available free of charge at https://pubs.acs.org/doi/10.1021/acsenergylett.1c01071.

Materials and methods (material synthesis, electrochemical characterization, materials characterization), XRD and NPD of NLMO and doped-NLMO, SEM images, pre-edge peaks of XANES spectra NLMO and doped-NLMO, XANES spectra of NLMO, RIXS maps of NLMO and doped-NLMO, fitted FT transformed EXAFS spectra of NLMO, separator images of NLMO and doped-NLMO, ICP-MS of NLMO, soft XAS spectra

https://doi.org/10.1021/acsenergylett.1c01071
ACS Energy Lett. 2021, 6, 2882−2890

of NLMO and doped-NLMO, electrochemical characterization of NLMO and doped-NLMO, lattice occupancy and lattice parameters of NLMO and doped-NLMO, ICP-MS quantification of dissolved Mn in separator from NLMO and doped-NLMO, EXAFS fitting parameters of NLMO and doped-NLMO (PDF)

AUTHOR INFORMATION

Corresponding Author

Feng Lin − *Department of Chemistry, Virginia Tech, Blacksburg, Virginia 24061, United States;* orcid.org/0000-0002-3729-3148; Email: fenglin@vt.edu

Authors

Muhammad Mominur Rahman − *Department of Chemistry, Virginia Tech, Blacksburg, Virginia 24061, United States;* orcid.org/0000-0001-6814-456X

Scott McGuigan − *Department of Chemistry, Virginia Tech, Blacksburg, Virginia 24061, United States*

Shaofeng Li − *Stanford Synchrotron Radiation Lightsource, SLAC National Accelerator Laboratory, Menlo Park, California 94025, United States*

Lina Gao − *Department of Chemistry, Zhejiang University, Hangzhou, Zhejiang 310027, China*

Dong Hou − *Department of Chemistry, Virginia Tech, Blacksburg, Virginia 24061, United States*

Zhijie Yang − *Department of Chemistry, Virginia Tech, Blacksburg, Virginia 24061, United States*

Zhengrui Xu − *Department of Chemistry, Virginia Tech, Blacksburg, Virginia 24061, United States;* orcid.org/0000-0002-6549-4713

Sang-Jun Lee − *Stanford Synchrotron Radiation Lightsource, SLAC National Accelerator Laboratory, Menlo Park, California 94025, United States;* orcid.org/0000-0002-8199-3993

Cheng-Jun Sun − *Advanced Photon Source, Argonne National Laboratory, Argonne, Illinois 60439, United States*

Jue Liu − *Oak Ridge National Laboratory, Oak Ridge, Tennessee 37830, United States;* orcid.org/0000-0002-4453-910X

Xiaojing Huang − *National Synchrotron Light Source II, Brookhaven National Laboratory, Upton, New York 11973, United States*

Xianghui Xiao − *National Synchrotron Light Source II, Brookhaven National Laboratory, Upton, New York 11973, United States*

Yong Chu − *National Synchrotron Light Source II, Brookhaven National Laboratory, Upton, New York 11973, United States*

Sami Sainio − *Stanford Synchrotron Radiation Lightsource, SLAC National Accelerator Laboratory, Menlo Park, California 94025, United States*

Dennis Nordlund − *Stanford Synchrotron Radiation Lightsource, SLAC National Accelerator Laboratory, Menlo Park, California 94025, United States*

Xueqian Kong − *Department of Chemistry, Zhejiang University, Hangzhou, Zhejiang 310027, China;* orcid.org/0000-0002-1901-9073

Yijin Liu − *Stanford Synchrotron Radiation Lightsource, SLAC National Accelerator Laboratory, Menlo Park, California 94025, United States*

Complete contact information is available at: https://pubs.acs.org/10.1021/acsenergylett.1c01071

Author Contributions

F.L. designed and conceived the project and assisted in manuscript preparation. M.M.R. synthesized materials, performed electrochemical analysis, XRD, XAS, X-ray fluorescence tomography, SEM-EDS data analysis, and manuscript preparation. S.M. assisted in materials synthesis. S.L., Y.L., and S.-J. Lee acquired and analyzed RIXS data. L.G. and X.K. acquired and analyzed ^{7}Li NMR data. D.H. analyzed neutron diffraction data. Z.Y., Z.X., and C.S. acquired hard XAS data. J.L. acquired neutron diffraction data. X.H., X.X., and Y.C. acquired fluorescence tomographs. S.S. and D.N. acquired soft XAS data.

Notes

The authors declare no competing financial interest.

ACKNOWLEDGMENTS

The work was supported by the National Science Foundation under no. CBET 1912885, as well as Virginia Tech College of Science Lay Nam Chang Dean's Discovery Fund. Use of the Stanford Synchrotron Radiation Lightsource, SLAC National Accelerator Laboratory, is supported by the U.S. Department of Energy, Office of Science, Office of Basic Energy Sciences, under Contract No. DE-AC02-76SF00515. This research used resources of the Advanced Photon Source; a U.S. Department of Energy (DOE) Office of Science User Facility operated for the DOE Office of Science by Argonne National Laboratory under Contract No. DE-AC02-06CH11357. Use of the resources of the National Synchrotron Light Source II is supported by Department of Energy (DOE), Office of Science User Facility operated for the DOE Office of Science by the Brookhaven National Laboratory under Contract No. DE-SC0012704. A portion of this research used resources at the Spallation Neutron Source, a DOE Office of Science User Facility operated by the Oak Ridge National Laboratory. The authors thank Stephanie Spence for data discussion. The authors also thank Dr. Yan-Yan Hu for the scientific discussion.

REFERENCES

(1) Assat, G.; Tarascon, J. M. Fundamental Understanding and Practical Challenges of Anionic Redox Activity in Li-Ion Batteries. *Nat. Energy* **2018**, *3* (5), 373−386.

(2) Rahman, M. M.; Lin, F. Oxygen Redox Chemistry in Rechargeable Li-Ion and Na-Ion Batteries. *Matter* **2021**, *4* (2), 490−527.

(3) Luo, K.; Roberts, M. R.; Hao, R.; Guerrini, N.; Pickup, D. M.; Liu, Y. S.; Edström, K.; Guo, J.; Chadwick, A. V.; Duda, L. C.; Bruce, P. G. Charge-Compensation in 3d-Transition-Metal-Oxide Intercalation Cathodes through the Generation of Localized Electron Holes on Oxygen. *Nat. Chem.* **2016**, *8* (7), 684−691.

(4) Koga, H.; Croguennec, L.; Ménétrier, M.; Mannessiez, P.; Weill, F.; Delmas, C. Different Oxygen Redox Participation for Bulk and Surface: A Possible Global Explanation for the Cycling Mechanism of Li1.20Mn 0.54Co0.13Ni0.13O2. *J. Power Sources* **2013**, *236*, 250−258.

(5) Seo, D.-H.; Lee, J.; Urban, A.; Malik, R.; Kang, S.; Ceder, G. The Structural and Chemical Origin of the Oxygen Redox Activity in Layered and Cation-Disordered Li-Excess Cathode Materials. *Nat. Chem.* **2016**, *8* (7), 692−697.

(6) Maitra, U.; House, R. A.; Somerville, J. W.; Tapia-Ruiz, N.; Lozano, J. G.; Guerrini, N.; Hao, R.; Luo, K.; Jin, L.; Pérez-Osorio, M. A.; Massel, F.; Pickup, D. M.; Ramos, S.; Lu, X.; McNally, D. E.; Chadwick, A. V.; Giustino, F.; Schmitt, T.; Duda, L. C.; Roberts, M. R.; Bruce, P. G. Oxygen Redox Chemistry without Excess Alkali-Metal

Ions in Na2/3[Mg0.28Mn0.72]O2. *Nat. Chem.* **2018**, *10* (3), 288−295.
(7) Wang, Q. C.; Meng, J. K.; Yue, X. Y.; Qiu, Q. Q.; Song, Y.; Wu, X. J.; Fu, Z. W.; Xia, Y. Y.; Shadike, Z.; Wu, J.; Yang, X. Q.; Zhou, Y. N. Tuning P2-Structured Cathode Material by Na-Site Mg Substitution for Na-Ion Batteries. *J. Am. Chem. Soc.* **2019**, *141* (2), 840−848.
(8) House, R. A.; Maitra, U.; Pérez-Osorio, M. A.; Lozano, J. G.; Jin, L.; Somerville, J. W.; Duda, L. C.; Nag, A.; Walters, A.; Zhou, K. J.; Roberts, M. R.; Bruce, P. G. Superstructure Control of First-Cycle Voltage Hysteresis in Oxygen-Redox Cathodes. *Nature* **2020**, *577* (7791), 502−508.
(9) Boulineau, A.; Simonin, L.; Colin, J.-F.; Bourbon, C.; Patoux, S. First Evidence of Manganese-Nickel Segregation and Densification upon Cycling in Li-Rich Layered Oxides for Lithium Batteries. *Nano Lett.* **2013**, *13* (8), 3857−3863.
(10) Rahman, M. M.; Chen, W. Y.; Mu, L.; Xu, Z.; Xiao, Z.; Li, M.; Bai, X. M.; Lin, F. Defect and Structural Evolution under High-Energy Ion Irradiation Informs Battery Materials Design for Extreme Environments. *Nat. Commun.* **2020**, *11* (1), 4548.
(11) House, R. A.; Maitra, U.; Jin, L.; Lozano, J. G.; Somerville, J. W.; Rees, N. H.; Naylor, A. J.; Duda, L. C.; Massel, F.; Chadwick, A. V.; Ramos, S.; Pickup, D. M.; McNally, D. E.; Lu, X.; Schmitt, T.; Roberts, M. R.; Bruce, P. G. What Triggers Oxygen Loss in Oxygen Redox Cathode Materials? *Chem. Mater.* **2019**, *31* (9), 3293−3300.
(12) Yang, L.; Li, X.; Liu, J.; Xiong, S.; Ma, X.; Liu, P.; Bai, J.; Xu, W.; Tang, Y.; Hu, Y.-Y.; Liu, M.; Chen, H. Lithium-Doping Stabilized High-Performance P2−Na $_{0.66}$ Li $_{0.18}$ Fe $_{0.12}$ Mn $_{0.7}$ O $_{2}$ Cathode for Sodium Ion Batteries. *J. Am. Chem. Soc.* **2019**, *141* (16), 6680−6689.
(13) Xu, J.; Lee, D. H.; Clément, R. J.; Yu, X.; Leskes, M.; Pell, A. J.; Pintacuda, G.; Yang, X.-Q.; Grey, C. P.; Meng, Y. S. Identifying the Critical Role of Li Substitution in P2−Na $_{x}$ [Li $_{y}$ Ni $_{z}$ Mn $_{1-y-z}$]O $_{2}$ (0 < *x*, *y*, *z* < 1) Intercalation Cathode Materials for High-Energy Na-Ion Batteries. *Chem. Mater.* **2014**, *26* (2), 1260−1269.
(14) Han, M. H.; Gonzalo, E.; Sharma, N.; López Del Amo, J. M.; Armand, M.; Avdeev, M.; Saiz Garitaonandia, J. J.; Rojo, T. High-Performance P2-Phase Na2/3Mn0.8Fe0.1Ti0.1O2 Cathode Material for Ambient-Temperature Sodium-Ion Batteries. *Chem. Mater.* **2016**, *28* (1), 106−116.
(15) Simonelli, L.; Sorrentino, A.; Marini, C.; Ramanan, N.; Heinis, D.; Olszewski, W.; Mullaliu, A.; Birrozzi, A.; Laszczynski, N.; Giorgetti, M.; Passerini, S.; Tonti, D. Role of Manganese in Lithium- and Manganese-Rich Layered Oxides Cathodes. *J. Phys. Chem. Lett.* **2019**, *10* (12), 3359−3368.
(16) Asl, H. Y.; Manthiram, A. Reining in Dissolved Transition-Metal Ions. *Science (Washington, DC, U. S.)* **2020**, *369* (6500), 140−141.
(17) Mu, L.; Zhang, R.; Kan, W. H.; Zhang, Y.; Li, L.; Kuai, C.; Zydlewski, B.; Rahman, M. M.; Sun, C.-J.; Sainio, S.; Avdeev, M.; Nordlund, D.; Xin, H. L.; Lin, F. Dopant Distribution in Co-Free High-Energy Layered Cathode Materials. *Chem. Mater.* **2019**, *31* (23), 9769−9776.
(18) Huang, Y.; Yan, Z.; Luo, W.; Hu, Z.; Liu, G.; Zhang, L.; Yang, X.; Ou, M.; Liu, W.; Huang, L.; Lin, H.; Chen, C.; Te; Luo, J.; Li, S.; Han, J.; Chou, S.; Huang, Y. Vitalization of P2−Na2/3Ni1/3Mn2/3O2 at High-Voltage Cyclability via Combined Structural Modulation for Sodium-Ion Batteries. *Energy Storage Mater.* **2020**, *29*, 182−189.
(19) Singh, G.; Gupta, S. L.; Prasad, R.; Auluck, S.; Gupta, R.; Sil, A. Suppression of Jahn-Teller Distortion by Chromium and Magnesium Doping in Spinel LiMn2O4: A First-Principles Study Using GGA and GGA+U. *J. Phys. Chem. Solids* **2009**, *70* (8), 1200−1206.
(20) Fang, T.; Guo, S.; Jiang, K.; Zhang, X.; Wang, D.; Feng, Y.; Zhang, X.; Wang, P.; He, P.; Zhou, H. Revealing the Critical Role of Titanium in Layered Manganese-Based Oxides toward Advanced Sodium-Ion Batteries via a Combined Experimental and Theoretical Study. *Small Methods* **2019**, *3* (4), 1800183.
(21) Steiner, J. D.; Cheng, H.; Walsh, J.; Zhang, Y.; Zydlewski, B.; Mu, L.; Xu, Z.; Rahman, M. M.; Sun, H.; Michel, F. M.; Sun, C.-J.; Nordlund, D.; Luo, W.; Zheng, J.-C.; Xin, H. L.; Lin, F. Targeted Surface Doping with Reversible Local Environment Improves Oxygen Stability at the Electrochemical Interfaces of Nickel-Rich Cathode Materials. *ACS Appl. Mater. Interfaces* **2019**, *11* (41), 37885−37891.
(22) Cheng, J.; Mu, L.; Wang, C.; Yang, Z.; Xin, H. L.; Lin, F.; Persson, K. A. Enhancing Surface Oxygen Retention through Theory-Guided Doping Selection in Li1-: XNiO2for next-Generation Lithium-Ion Batteries. *J. Mater. Chem. A* **2020**, *8* (44), 23293−23303.
(23) Yabuuchi, N.; Hara, R.; Kajiyama, M.; Kubota, K.; Ishigaki, T.; Hoshikawa, A.; Komaba, S. New O2/P2-Type Li-Excess Layered Manganese Oxides as Promising Multi-Functional Electrode Materials for Rechargeable Li/Na Batteries. *Adv. Energy Mater.* **2014**, *4* (13), 1301453.
(24) Delmas, C.; Braconnier, J. J.; Fouassier, C.; Hagenmuller, P. Electrochemical Intercalation of Sodium in NaxCoO2 Bronzes. *Solid State Ionics* **1981**, *3*−*4* (C), 165−169.
(25) Yang, Z.; Mu, L.; Hou, D.; Rahman, M. M.; Xu, Z.; Liu, J.; Nordlund, D.; Sun, C.; Xiao, X.; Lin, F. Probing Dopant Redistribution, Phase Propagation, and Local Chemical Changes in the Synthesis of Layered Oxide Battery Cathodes. *Adv. Energy Mater.* **2021**, *11* (1), 2002719.
(26) Buchholz, D.; Li, J.; Passerini, S.; Aquilanti, G.; Wang, D.; Giorgetti, M. X-Ray Absorption Spectroscopy Investigation of Lithium-Rich, Cobalt-Poor Layered-Oxide Cathode Material with High Capacity. *ChemElectroChem* **2015**, *2* (1), 85−97.
(27) Yang, W.; Devereaux, T. P. Anionic and Cationic Redox and Interfaces in Batteries: Advances from Soft X-Ray Absorption Spectroscopy to Resonant Inelastic Scattering. *J. Power Sources* **2018**, *389*, 188−197.
(28) Zhuo, Z.; Pemmaraju, C.; Das; Vinson, J.; Jia, C.; Moritz, B.; Lee, I.; Sallies, S.; Li, Q.; Wu, J.; Dai, K.; Chuang, Y.; Hussain, Z.; Pan, F.; Devereaux, T. P.; Yang, W. Spectroscopic Signature of Oxidized Oxygen States in Peroxides. *J. Phys. Chem. Lett.* **2018**, *9* (21), 6378−6384.
(29) Wu, J.; Zhuo, Z.; Rong, X.; Dai, K.; Lebens-Higgins, Z.; Sallis, S.; Pan, F.; Piper, L. F. J.; Liu, G.; Chuang, Y.; Hussain, Z.; Li, Q.; Zeng, R.; Shen, Z.; Yang, W. Dissociate Lattice Oxygen Redox Reactions from Capacity and Voltage Drops of Battery Electrodes. *Sci. Adv.* **2020**, *6* (6), eaaw3871.
(30) Dai, K.; Wu, J.; Zhuo, Z.; Li, Q.; Sallis, S.; Mao, J.; Ai, G.; Sun, C.; Li, Z.; Gent, W. E.; Chueh, W. C.; Chuang, Y.; Zeng, R.; Shen, Z.; Pan, F.; Yan, S.; Piper, L. F. J.; Hussain, Z.; Liu, G.; Yang, W. High Reversibility of Lattice Oxygen Redox Quantified by Direct Bulk Probes of Both Anionic and Cationic Redox Reactions. *Joule* **2019**, *3* (2), 518−541.
(31) Ravel, B.; Newville, M. ATHENA and ARTEMIS: Interactive Graphical Data Analysis Using IFEFFIT. *Phys. Scr.* **2005**, *T115* (T115), 1007−1010.
(32) Clément, R. J.; Xu, J.; Middlemiss, D. S.; Alvarado, J.; Ma, C.; Meng, Y. S.; Grey, C. P. Direct Evidence for High Na+ Mobility and High Voltage Structural Processes in P2-Nax[LiyNizMn1-y-z]O2 (x, y, $z \leq 1$) Cathodes from Solid-State NMR and DFT Calculations. *J. Mater. Chem. A* **2017**, *5* (8), 4129−4143.
(33) Chen, Q.; Pei, Y.; Chen, H.; Song, Y.; Zhen, L.; Xu, C. Y.; Xiao, P.; Henkelman, G. Highly Reversible Oxygen Redox in Layered Compounds Enabled by Surface Polyanions. *Nat. Commun.* **2020**, *11* (1), 3411.
(34) Cao, X.; Li, X.; Qiao, Y.; Jia, M.; Qiu, F.; He, Y.; He, P.; Zhou, H. Restraining Oxygen Loss and Suppressing Structural Distortion in a Newly Ti-Substituted Layered Oxide P2-Na $_{0.66}$ Li $_{0.22}$ Ti $_{0.15}$ Mn $_{0.63}$ O $_{2}$. *ACS Energy Lett.* **2019**, *4* (10), 2409−2417.
(35) Li, C.; Zhao, C.; Hu, B.; Tong, W.; Shen, M.; Hu, B. Unraveling the Critical Role of Ti Substitution in P2-NaxLiyMn1-YO2 Cathode for Highly Reversible Oxygen Redox Chemistry. *Chem. Mater.* **2020**, *32* (3), 1054−1063.
(36) Zhang, K.; Kim, D.; Hu, Z.; Park, M.; Noh, G.; Yang, Y.; Zhang, J.; Lau, V. W.; Chou, S.-L.; Cho, M.; Choi, S.-Y.; Kang, Y.-M. Manganese Based Layered Oxides with Modulated Electronic and Thermodynamic Properties for Sodium Ion Batteries. *Nat. Commun.* **2019**, *10* (1), 5203.

https://doi.org/10.1021/acsenergylett.1c01071
ACS Energy Lett. 2021, 6, 2882−2890

(37) Günter, F. J.; Habedank, J. B.; Schreiner, D.; Neuwirth, T.; Gilles, R.; Reinhart, G. Introduction to Electrochemical Impedance Spectroscopy as a Measurement Method for the Wetting Degree of Lithium-Ion Cells. *J. Electrochem. Soc.* **2018**, *165* (14), A3249−A3256.
(38) Rahman, M. M.; Mao, J.; Kan, W. H.; Sun, C.-J.; Li, L.; Zhang, Y.; Avdeev, M.; Du, X.-W.; Lin, F. An Ordered P2/P3 Composite Layered Oxide Cathode with Long Cycle Life in Sodium-Ion Batteries. *ACS Mater. Lett.* **2019**, *1* (5), 573−581.

https://doi.org/10.1021/acsenergylett.1c01071
ACS Energy Lett. 2021, 6, 2882−2890